Real-Time Intravascular Shear Stress in the Rabbit Abdominal Aorta

Lisong Ai, Hongyu Yu, *Member, IEEE*, Wangde Dai, Sharon L. Hale, Robert A. Kloner, and Tzung K. Hsiai*

***Abstract*—Fluid shear stress is intimately linked with the biological activities of vascular cells. A flexible microelectromechanical system (MEMS) sensor was developed to assess spatial- and temporal-varying components of intravascular shear stress (ISS) in the abdominal aorta of adult New Zealand white (NZW) rabbits. Real-time ISS ($ISS_{real\text{-}time}$) was analyzed in comparison with computational fluid dynamics (CFD) simulations for wall shear stress (WSS). Three-dimensional abdominal arterial geometry and mesh were created using the GAMBIT software. Simulation of arterial flow profiles was established by FLUENT. The Navier–Stokes equations were solved for non-Newtonian blood flow. The coaxial-wire-based MEMS sensor was deployed into the abdominal arteries of rabbits via a femoral artery cutdown. Based on the CFD analysis, the entrance length of the sensor on the coaxial wire (0.4 mm in diameter) was less than 10 mm. Three-dimensional fluoroscope and contrast dye allowed for visualization of the positions of the sensor and ratios of vessel to coaxial wire diameters. Doppler ultrasound provided the velocity profiles for the CFD boundary conditions. If the coaxial wire were positioned at the center of vessel, the CFD analysis revealed a mean ISS value of 31.1 with a systolic peak at 102.8 dyn $\cdot$ cm^{-2}. The mean WSS was computed to be 10.1 dyn $\cdot$ cm^{-2} with a systolic peak at 33.2 dyn $\cdot$ cm^{-2}, and the introduction of coaxial wire increased the mean WSS by 5.4 dyn $\cdot$ cm^{-2} and systolic peak by 18.0 dyn $\cdot$ cm^{-2}. Experimentally, the mean ISS was 11.9 dyn $\cdot$ cm^{-2} with a systolic peak at 47.0 dyn $\cdot$ cm^{-2}. The waveform of experimental ISS was similar to that of CFD solution with a 30.2% difference in mean and 8.9% in peak systolic shear stress. Despite the difference between CD and experimental results, the flexible coaxial-wire-based MEMS sensors provided a possibility to assess real-time ISS in the abdominal aorta of NZW rabbits.**

Manuscript received June 5, 2008; revised September 6, 2008 and November 26, 2008. Current version published June 10, 2009. This work was supported in part by the American Heart Association (AHA) GIA 0655051Y (TKH), NIH HL 83015 (TKH), and NIH HL068689 (TKH), in part by the American Heart Association Postdoctoral Fellowship 0725016Y (HY), and in part by the AHA Predoctoral Fellowship 0615063Y (MR). *Asterisk indicates corresponding author.*

L. Ai is with the Department of Biomedical Engineering and Cardiovascular Medicine, University of Southern California, Los Angeles, CA 90089-1111 USA.

H. Yu is with the Department of Biomedical Engineering and Cardiovascular Medicine, University of Southern California, Los Angeles, CA 90089-1111 USA, and also with the School of Earth and Space Exploration and the Electrical Engineering Department, Arizona State University, Tempe, AZ 85287-9309 USA.

W. Dai is with the Heart Institute, Good Samaritan Hospital, Los Angeles, CA 90017, USA, and also with the Keck School of Medicine, University of Southern California, Los Angeles, CA 90089 USA.

S. L. Hale is with the Heart Institute, Good Samaritan Hospital, Los Angeles, CA 90017 USA.

R. A. Kloner is with the Heart Institute, Good Samaritan Hospital, Los Angeles, CA 90017, USA, and also with the Cardiovascular Division, Keck School of Medicine, University of Southern California, Los Angeles, CA 90089 USA.

*T. K. Hsiai is with the Department of Biomedical Engineering and Cardiovascular Medicine, University of Southern California, Los Angeles, CA 90089-1111 USA (e-mail: hsiai@usc.edu).

Color versions of one or more of the figures in this paper are available online at http://ieeexplore.ieee.org.

Digital Object Identifier 10.1109/TBME.2009.2013455

***Index Terms*—Computational fluid dynamics (CFD), intravascular shear stress (ISS), microelectromechanical system (MEMS) sensors.**

I. Introduction

FLUID shear stress modulates the genotypic and phenotypic expression of vascular cells. Developmentally, fluid shear stress is an epigenetic factor for zebra fish embryonic cardiac tube formation [1]. Absence of fluid flow resulted in abnormal cardiac chambers and valve formation [2]. Disturbed flow is also a stimulus for morphologic embryonic heart. The direction of fluid shear stress in the node of mouse embryos determines the left–right asymmetry in the body plan [3]. A line of evidence supports that fluid shear stress influences the differentiation of embryonic stem cells [4], mesenchymal progenitor cells [5], and human bone-marrow-derived progenitors to endothelial cells [1]. Thus, the role of fluid shear stress spans from developmental biology to cardiovascular health.

Equally important are the spatial and temporal variations of shear stress on vascular cells [6]. Physical exercise augments fluid shear stress and confers a salutary endothelial cell function [7]. Disturbed flow, including oscillatory shear stress (bidirectional net zero forward flow), is considered to be atherogenic, developing on the lateral wall of arterial bifurcation, whereas pulsatile flow is atheroprotective, developing on the medial wall of bifurcation or straight segments [8], [9]. Identification of arterial regions of low wall shear stress (WSS) would predict progression of atherosclerosis [10], localization of high-risk coronary atherosclerotic plaques, vessel wall remodeling [11], and abdominal aortic aneurysm (AAA) [12], [13]. Furthermore, identification of specific regions in the prosthetic valve leaflets [14], the cardiopulmonary bypass machine [15], and left ventricular assist device (LVAD) would predict thrombus formation [16]. In this context, the ability to measure real-time shear stress would advance the field of cardiovascular research.

The advent of microelectromechanical systems (MEMSs) has opened the possibility to assess spatial and temporal variations in shear stress *in vitro* [17], [18]. Development of flexible sensors and actuators has further enabled us to assess the spatial- and temporal-varying components of intravascular shear stress (ISS) *in vivo* [19]–[22]. Recently, we have microfabricated the polymer-based sensors for real-time ISS assessment in the New Zealand white (NZW) rabbits [23], [24].

We compared computational fluid dynamics (CFD) derived shear stress simulation with the MEMS sensor-acquired real-time ISS. In parallel, we analyzed the effects of MEMS sensor dimension, position, and orientation in relation to the abdominal aorta of NZW rabbits. We observed that the systolic and

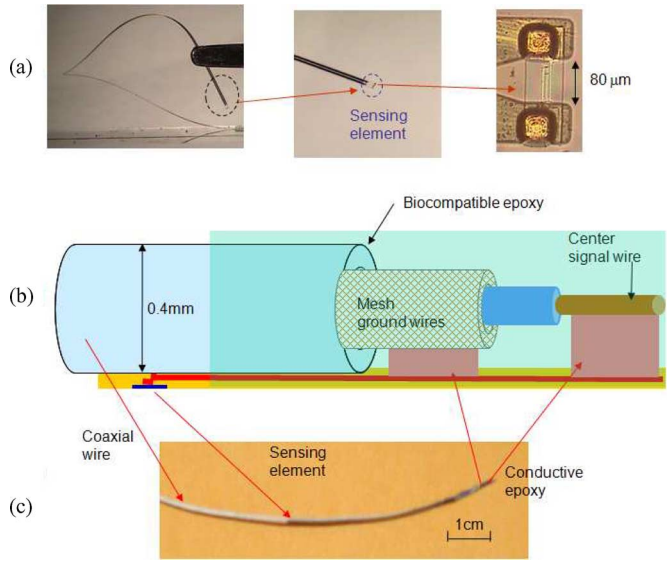

Fig. 1. Flexible intravascular sensors. (a) Sensor was bended or folded without structural or functional damage. The sensing element was positioned at the tip of the sensor, and the sensing element was made of 2-μm-wide Ti/Pt strip with a dimension of 280 μm. (b) Sensor was packaged to the electrical coaxial wire with conductive epoxy and covered with biocompatible epoxy to prevent from electrical current leakage. The distance between the sensing element and the tip of the catheter was 4 cm, which was designed based on entrance length to avoid flow disturbance. (c) Packaged sensor (black color) on electrical coaxial wire (white color).

diastolic component of real-time ISS ($ISS_{\text{real-time}}$) waveforms resembled those of computed ISS and WSS. If the coaxial wire were positioned at the center of vessel, the CFD analysis revealed a mean ISS value of 31.2 with a systolic peak at 102.8 dyn $\cdot$ cm^{-2}. The mean WSS was computed to be 10.1 dyn $\cdot$ cm^{-2} with a systolic peak at 33.2 dyn $\cdot$ cm^{-2}, and the introduction of coaxial wire increased the mean WSS to 15.5 dyn $\cdot$ cm^{-2} and systolic peak to 45.5 dyn $\cdot$ cm^{-2}. Experimentally, the mean $ISS_{\text{real-time}}$ was measured at 11.9 dyn $\cdot$ cm^{-2} with a systolic peak at 47.0 dyn $\cdot$ cm^{-2}. The difference between the mean magnitudes of $ISS_{\text{real-time}}$ (11.9 dyn $\cdot$ cm^{-2}) and WSS_{catheter} (15.5 dyn $\cdot$ cm^{-2}) was 3.6 dyn $\cdot$ cm^{-2}. Hence, our MEMS sensors provided the possibility to assess experimental ISS in the abdominal aorta of NZW rabbits.

II. Methods

A. Catheter-Based Polymer Sensors

1) Microfabrication and Packaging: The sensor was fabricated using surface micromachining with biocompatible materials including Parylene C, Ti, and Pt. The detailed fabrication process of the MEMS sensor was discussed by Yu *et al.* [25]. The individual sensing elements were 4 cm in length, 320 μm in width, and 21 μm in thickness [Fig. 1(a)]. Ti and Pt offered biocompatibility for the heating and sensing component of the sensor. The Ti/Pt sensing element (160 μm in length by 80 μm in width) was encapsulated in parylene polymer in direct contact with the blood flow.

The sensors were integrated onto an electrical coaxial wire (Precision Interconnect, Portland, OR) as a catheter's guide wire application for ISS analysis [Fig. 1(b)]. The coaxial wire was 0.4 mm in diameter and the sensor body is 4.0 cm in length. The sensing element was 80 μm in width and 240 μm in length. The wire bonding sites of the Cr/Au electrode leads were connected to the coaxial wire tip using the biocompatible conductive epoxy (EPO-TEK H20E; Epoxy Technology, Billerica, MA), and were cured at 90 °C over 3 h. The biocompatible epoxy (EPO-TEK 301; Epoxy Technology, Billerica, MA) anchored the sensor body on the coaxial wire surface [Fig. 1(c)].

2) In Vivo Assessment of Intravascular Shear Stress: We tested the feasibility of acquiring real-time shear stress measurements from the NZW rabbit's aorta, specifically, abdominal aorta and aortic arch. Deployment of the polymer device into the rabbit's aorta was performed in compliance with the Institutional Animal Care and Use Committee in the Heart Institute of the Good Samaritan Hospital (Los Angeles, CA), which is accredited by the American Association for Accreditation for Laboratory Animal Care.

Five male NZW rabbits (ten weeks, mean body weight 2442 ± 210 g) were acquired from a local breeder (Irish Farms, Norco, CA) and maintained in the Good Samaritan Hospital Vivarium in accordance with the National Institutes of Health guidelines. After a seven-day quarantine period, the rabbits were anesthetized for percutaneous access according to the institutional review committee, and anesthesia was induced through an intramuscular injection of 50 mg/kg ketamine (JHP Pharmaceuticals, LLC) combined with 10 mg/kg xylazine (IVX Animal Health, Inc.). A 23-gauge hypodermic needle and a 26-gauge guide wire were introduced into the left femoral artery via a cutdown. A rabbit femoral catheter (0.023 in ID $\times$0.038 in OD) was passed through the left femoral artery. The circulatory system of the individual animals was anticoagulated with heparin (100 units/kg) prior to the sensor deployment. The catheters and needles were rinsed with heparin at 1000 units/mL prior to the procedure.

An ultrasound transducer (Philips SONOS 5500 at 12 MHz) was positioned over the abdomen to interrogate arterial blood flow. Periodic blood pressure measurement was obtained with an automated tail cuff (IITC/Life Science Instruments). Using the fluoroscope in the animal angiographic laboratory (Phillips BV-22HQ C-arm), the operator was able to visualize and steer the coaxial wire in the aorta of the NZW rabbit to the abdominal aorta [Fig. 2(a)]. Contrast dye was injected to delineate the position of the coaxial wire in relation to the inner aortic diameter [Fig. 2(b)]. The voltage recordings were synchronized with the rabbit's cardiac cycle via ECG (The ECGenie, Mouse Specifics). After the measurement, the coaxial wire was removed and the femoral artery was tied off.

3) Data Acquisition: The constant current circuit was used for real-time voltage signal acquisition in the aorta. The input electrical current of 0.9833 mA was generated from a Multimeter (HP34401A, Santa Clara, CA), operating at a resistance measurement mode. When the current passed through the sensor, sensing element was heated up at an overheat ratio of $\sim$3%. The voltage cross of the sensing element was monitored by a LabVIEW-based data acquisition system, including a data acquisition board (NI USB-6251, Austin, TX) and a BNC adaptor

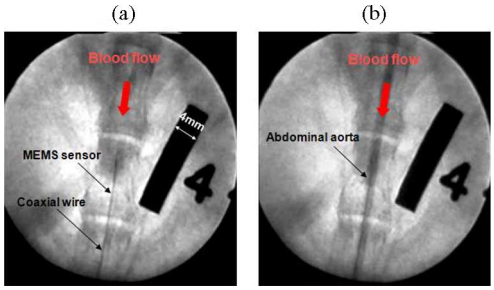

Fig. 2. Fluoroscopic images of *in vivo* testing of the MEMS sensor. (a) Catheter-based MEMS polymer sensor was visualized in the abdominal aorta of NZW rabbit. (b) Contrast dye was injected to delineate the diameter of the aorta in relation to the position of the catheter.

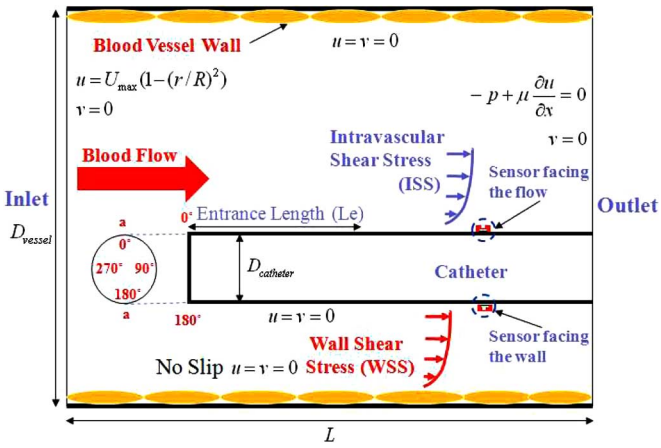

Fig. 3. Schematic diagram illustrates the geometry and boundary conditions for computational simulation to validate the *in vivo* ISS measurement and study its relation to the WSS on the vessel wall, where u and v represent the axial and radial velocities, D_{catheter} represents the catheter diameter, and L is the vessel length. The direction of blood flow is indicated by the red arrow.

board (BNC-2110, Austin, TX). The data acquisition system was connected to a laptop computer (ThinkPad T61, Lenovo, China) loaded with LabVIEW. The acquisition sampling rate was 800 Hz and the signal-to-noise ratio was 4.8. Wavelet decomposition and low-pass filters were applied to remove the noise background.

B. Computational Fluid Dynamics

1) Generation of 3-D Geometries and Meshes: The flow field was solved under three catheter positioning schemes: 1) at the center; 2) near the wall (0.1 mm away from the wall); and 3) 0.2 mm off the center. The inner diameter D_{vessel} of rabbit abdominal aorta was 2.4 mm as determined by injecting the contrast dye from the carotid artery. The wire bonding sites were integrated to the tip of the coaxial wire, and the sensing element was 4.0 cm downstream from the catheter tip. In the computational model, the vessel length L was set to be 6.0 cm and the catheter tip was facing the direction of flow and its tip was positioned at 1.0 cm downstream from the inlet to allow for fully developed flow [26], [27]. Important parameters in our CFD simulations were the catheter diameters (D_{catheter}) of 0.25 mm (OD of mouse catheter: 0.010 in), 0.4 mm (coaxial wire), and 0.97 mm (OD of dog catheter: 0.038 in). The geometry of the computational model is illustrated in Fig. 3, where u and v represent the axial and radial velocities and D_{catheter} the catheter diameter. The direction of blood flow is indicated by the red arrow. The entrance length is considered as the distance from the catheter tip in which the local shear stress value on the coaxial wire is higher than the shear stress in the fully developed region. Hence, the CFD results guided the position of our sensor to circumvent flow disturbance.

The entire luminal geometrical models were generated and meshed in a specialized preprocessing program (Fluent, Inc., Gambit 2.3.16, Lebanon, NH). A mesh consisting primarily of tetrahedral finite element was generated for the individual models. The grid was created by first grading the edges of the specified "source" faces with appropriate numbers of nodes followed by generating the surface meshes using PAVE scheme. Next, the volume mesh was generated using the Cooper meshing scheme to sweep the mesh node patterns of specified "source" faces through the volume [28]. The meshed models were imported into the main CFD solver (Fluent, Inc., Fluent 6.2.16, Lebanon, NH) for flow simulation.

2) Simulation of Blood Flow and Boundary Conditions: The blood flow was modeled by applying the 3-D Navier–Stokes equations. The governing equations, including mass and momentum equations, were solved for laminar, incompressible, and non-Newtonian flow. The arterial walls and the catheters were considered to be rigid and impermeable.

The equations describing laminar incompressible flow fields include the conservation of mass and momentum

$$\nabla \cdot \vec{u} = 0 \tag{1}$$

$$\frac{\partial \vec{u}}{\partial t} + (\vec{u} \cdot \nabla)\vec{u} = \frac{1}{\rho}\left(-\nabla p + \nabla \cdot \vec{\vec{\tau}}\right) \tag{2}$$

where $\vec{u}$ is the velocity vector, p is the pressure, and ρ is the fluid density. The density of rabbit blood is $\rho = 1055$ kg/m^3 [29]. The shear stress tensor in (2) is defined as

$$\vec{\vec{\tau}} = \mu(\dot{\gamma}) \cdot \dot{\gamma} \tag{3}$$

where μ is the absolute viscosity and $\dot{\gamma}$ is the local shear rate. The local shear rate $\dot{\gamma}$ was computed from the second scalar invariant of the rate of deformation tensor

$$\dot{\gamma} = \nabla \vec{u} + (\nabla \vec{u})^T. \tag{4}$$

Lorenzini [30] studied the differential viscous behavior between the Newtonian and non-Newtonian models and described the dynamic complexity of catheter-induced flow disturbance and the recirculation downstream from the catheter tip. The shear-rate-dependent absolute viscosity (μ) was calculated using the Carreau model to represent shear-thinning behavior of the rabbit blood [31], [32]

$$\mu(\dot{\gamma}) = \mu_\infty + \frac{\mu_0 - \mu_\infty}{[1 + (\lambda\dot{\gamma})^2]^{(1-n)/2}} \tag{5}$$

where μ_0 is the rate limit viscosity at zero shear rate, μ_∞ is the rate limit viscosity at infinite shear rate, λ is the relaxation

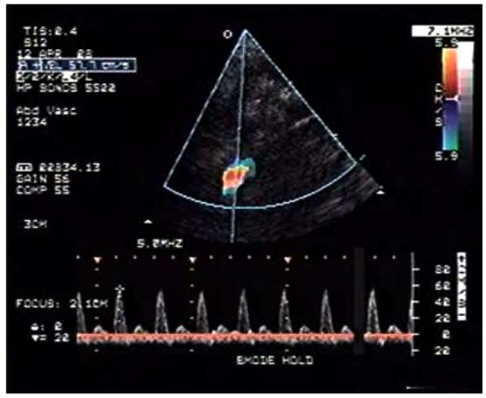

(a)

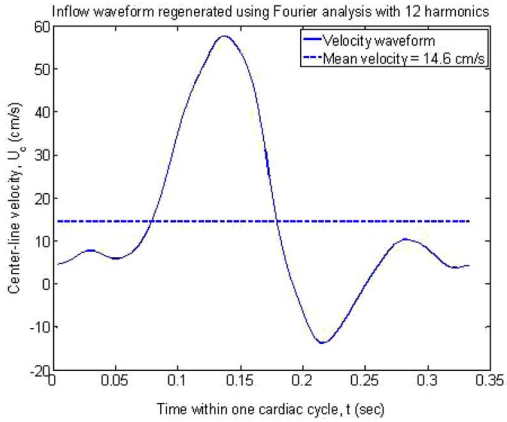

(b)

Fig. 4. Pulsatile velocity waveform was derived from Doppler ultrasound measurement. (a) Red-coded jets on color Doppler in upper panel aided the identification of abdominal arterial flow. The centerline velocity profile was recorded in the lower panel. (b) Recorded velocity profile was reconstructed with 12 harmonics by applying Fourier analysis.

time constant, and n is the power law index. To incorporate the non-Newtonian property of rabbit blood, four parameters were empirically determined as follows [29]:

1) $\mu_0 = 0.01937$ kg/m $\times$ s;
2) $\mu_\infty = 0.00345$ kg/m $\times$ s;
3) $\lambda = 1.3954$ s;
4) $n = 0.4816$.

Under no-slip conditions at the arterial wall, the spatial WSS, τ_w, was calculated for incompressible fluids from (3) as

$$\tau_w = -\mu_w \cdot \left.\frac{\partial u_t}{\partial n}\right|_{\text{wall}} \tag{6}$$

where μ_w is the dynamic viscosity at the wall, u_t is the velocity tangential to the wall, and n is the unit vector perpendicular to the wall.

The pulsatile velocity waveform for the inlet boundary condition was obtained from the Doppler ultrasound measurement. The ultrasound transducer was positioned over the abdomen to interrogate blood flow in the abdominal aorta [33]. The red-coded jets on color Doppler aided the identification of abdominal arterial flow [Fig. 4(a)]. The recorded profile of the centerline velocity U_c [Fig. 4(a)] was reconstructed with 12 harmonics by applying Fourier analysis to the measured data [Fig. 4(b)]. The period of one cardiac cycle T was 0.33 s corresponding to a heart rate at 180 beats/min. The mass flux calculated based on the velocity measurement was applied as the transient inlet boundary condition and implemented by a user-defined C++ code in FLUENT. The inlet Reynolds number Re calculated from the mean velocity was given by

$$\text{Re} = \frac{\rho U_{\text{mean}} D_{\text{vessel}}}{\mu} \tag{7}$$

where U_{mean} is the mean flow velocity at the inlet, which is half of the centerline velocity U_c under the assumption of parabolic velocity profile. The maximum and the time-averaged mean Re were calculated to be 204 and 52, respectively.

3) Finite-Volume Analysis: FLUENT uses a control-volume-based technique to convert the governing equations to algebraic equations that are solved numerically. This control volume technique consists of integrating the governing equations about each control volume, yielding discrete equations that conserve each quantity on a control volume basis [34]. The current simulations utilized a segregated solver and a pressure gradient adaptation technique to solve the governing equations sequentially. The second-order implicit formulation of the solver was applied for the unsteady simulations. Second-order upwind discretization was applied for the momentum equations. The pressure–velocity coupling was based on the SIMPLEC technique [34]. The numerical codes were used to calibrate the microsensor and simulate physiologic blood flow profiles and shear stress patterns.

III. Results

A. Computational Results

The catheter diameters and positions in the blood vessel impact on the physical parameters of blood flow. At a given inlet Reynolds number of 116 and vessel to catheter diameter ratios ($D_{\text{vessel}}/D_{\text{catheter}}$) of 2.5, the disturbance to velocity profiles in the straight vessel was notable (Fig. 5). At D_{vessel} to D_{catheter} ratio of 9.5, the flow disturbance was relatively small. When the catheter was positioned against the wall, the flow disturbance was also small.

ISS from the sensor was analyzed and compared with WSS. When the catheter was positioned in the center, a uniformly distributed shear stress pattern ($\text{ISS}_{\text{center}}$) developed along the catheter at a given entrance length (Fig. 3). At a $D_{\text{vessel}}/D_{\text{catheter}}$ ratio of 6 and Reynolds number of 116, $\text{ISS}_{\text{center}}$ (59.46 dyn $\cdot$ cm^{-2}) was greater than WSS (30.89 dyn $\cdot$ cm^{-2}) by 28.57 dyn $\cdot$ cm^{-2}.

The presence of the catheter also increased the flow resistance and WSS [30], [35]–[38]. The effects of the catheter that are positioned in the center of vessel on WSS and ISS in relation to Reynolds numbers are shown in Fig. 6(a) and (b). The presence of catheter elevated the arterial WSS by $\sim$30% for a catheter with a small diameter ($D_{\text{vessel}}/D_{\text{catheter}} = 9.5$) and by $\sim$144% for a large diameter ($D_{\text{vessel}}/D_{\text{catheter}} = 2.5$) [Fig. 6(a)]. The increase in ISS values was linearly proportional to the increase in Reynolds numbers [Fig. 6(b)]. Hence, the

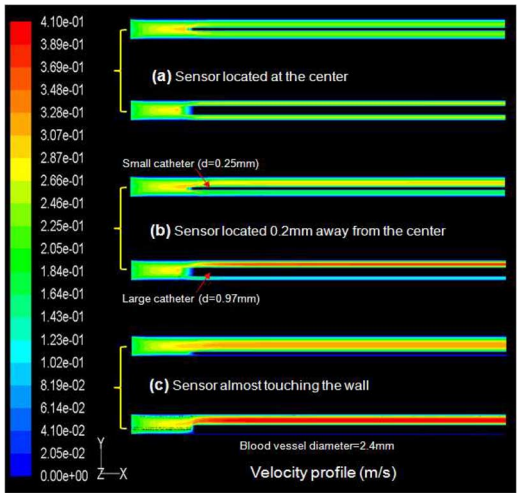

Fig. 5. Velocity profiles for two different catheter diameters and positions in a given vessel. (a) Catheter was positioned at the center. (b) Catheter was nearly in contact with the wall (0.1 mm away from the wall). (c) Catheter was at 0.2 mm away from the center. Small catheters introduced a small effect on changes in velocity profiles. The changes in velocity profiles became smaller as the catheter was steered toward the wall. The changes in velocity profiles were also small when the catheter was small and positioned near the wall.

ratios of $D_{\text{vessel}}/D_{\text{catheter}}$ influenced WSS, ISS, and the flow rate.

Similarly, ISS values varied circumferentially at 0°, 90°, 180°, and 270° when the catheter was off the vessel center [Fig. 3 and Fig. 7(a) and (b)]. Given a $D_{\text{vessel}}/D_{\text{catheter}}$ ratio of 9.5, a Reynolds number of 204, and a catheter position at 0.1 mm off the wall, the peak systolic ISS value was 22.0 dyn $\cdot$ cm^{-2} at 180° corresponding to the sensor facing the wall versus 100.8 dyn $\cdot$ cm^{-2} at 0° corresponding to the sensor facing the blood flow. The peak systolic WSS was 13.34 dyn $\cdot$ cm^{-2} on the side close to the catheter (180°) and 44.02 dyn $\cdot$ cm^{-2} on the side away from the catheter (0°). These differences became more pronounced in the presence of a large diameter ratio ($D_{\text{vessel}}/D_{\text{catheter}} = 6$). The peak systolic ISS values increased by 18-fold and that of WSS increased to 10.5 dyn $\cdot$ cm^{-2} at 180° and 191.1 dyn $\cdot$ cm^{-2} at 0°. This CFD prediction corroborated the importance of sensor positioning for ISS measurements. This prediction was also consistent with the previous finding that the existence of an additional boundary layer as a result of catheter decreased velocity and shear rate near the catheter, and the opposite applied when it was distant from the catheter [39].

Furthermore, positioning of the sensor on the small catheter was critical for real-time ISS measurement (Fig. 3). CFD simulations were performed at the peak systolic inlet Reynolds numbers in the rabbit abdominal aorta ($\text{Re}_{\text{max\_rabbit}} = 204$), and the entrance length was less than 6 mm [40]. We positioned the sensor at 4.0 cm downstream to minimize flow disturbance around the catheter tip.

B. Experimental Results

The position of the catheter influenced *in vivo* ISS measurements. When the catheter was positioned off the center, as shown in Fig. 3, the voltage signals varied significantly. Two distinct

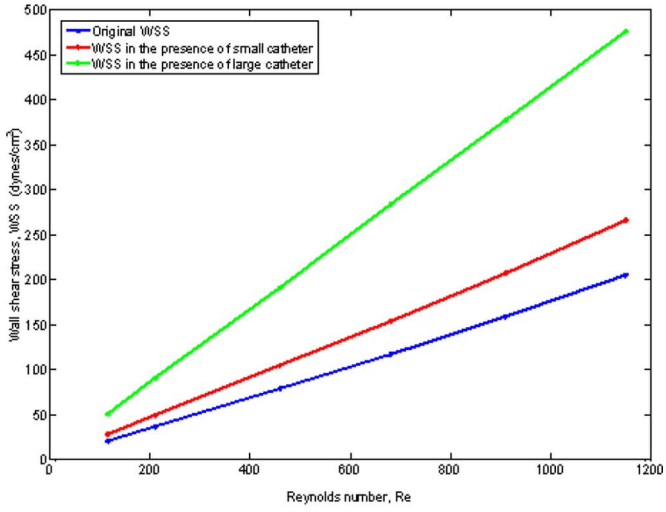

(a)

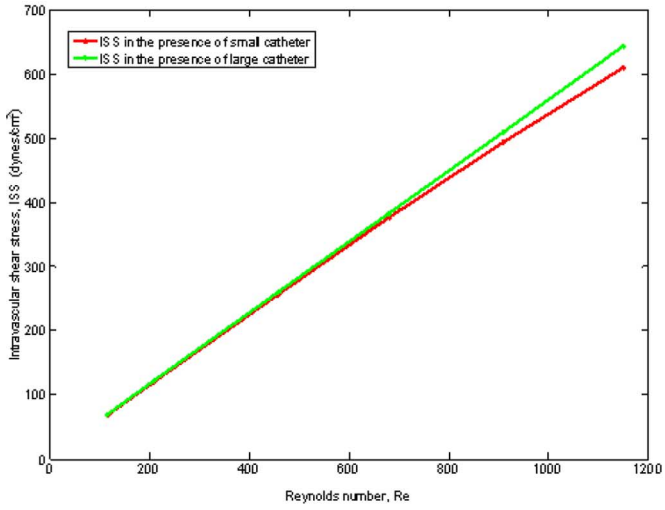

(b)

Fig. 6. Effects of the catheter on WSS and ISS in relation to various Reynolds numbers when the catheter was positioned at the center. (a) Presence of catheter elevated the arterial WSS by $\sim$30% for catheters with small diameter (OD = 0.97 mm) and by $\sim$144% for large diameter (OD = 0.25 mm). (b) Computed ISS increased linearly with the Reynolds numbers.

voltage waveforms were acquired in response to sensor facing the flow field versus the vessel wall (Fig. 8). High and pulsating signals were observed in the former position [Fig. 8(a)] and attenuated signals were recorded in the latter position [Fig. 8(b)]. The voltage signals were further attenuated when the flow ceased [Fig. 8(c)]. These findings were consistent with the predictions by our previous CFD simulation.

To translate WSS measurement from an *in vitro* bifurcating model [41] to animal models, we analyzed real-time ISS measurement with those of CFD codes. The catheter-based polymer sensor allowed for real-time acquisition of ISS in response to pulsatile arterial flow in the NZW rabbits. The representative *in vivo* voltage signals in the abdominal aorta were converted to shear stress using the calibration curve [25]. The bisection of the aorta and division of aortic segments from the NZW rabbit were illustrated to indicate the segments where ISS was

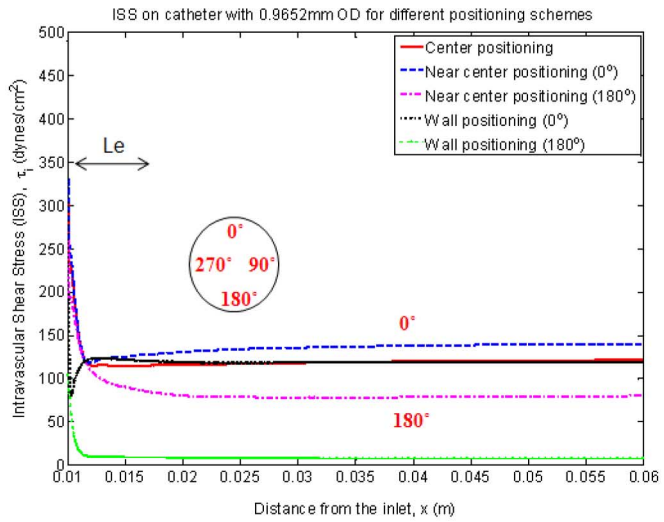

(a)

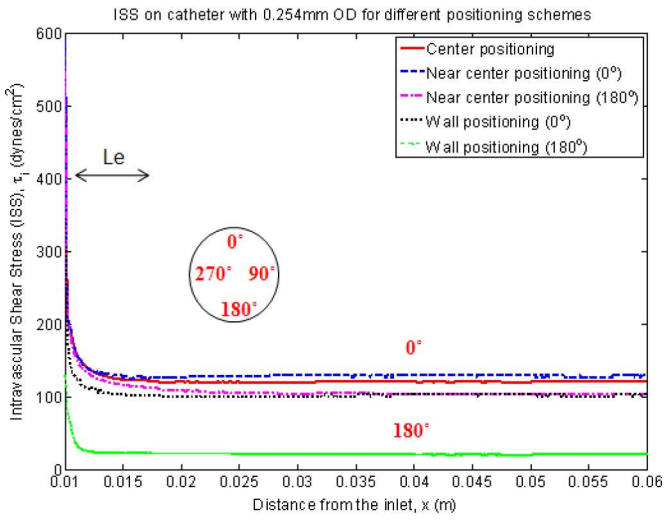

(b)

Fig. 7. Wall positioning led to a large variation in ISS measurements from the side facing the wall to the side facing the blood flow at a given flow rate (Re = 204). (a) ISS on the catheter with a large diameter (OD = 0.97 mm). (b) ISS on the catheter with a small diameter (OD = 0.25 mm).

acquired [Fig. 9(a)]. Two distinct output voltage waveforms were acquired near the aortic arch and the straight region of the abdominal aorta was recorded [Fig. 9(b) and (c)]. Our analyses focused on abdominal aorta.

Unsteady CFD simulations were performed to compare real-time ISS measurements in the context of the catheter diameter and position in the abdominal aorta. By applying the wavelet decomposition, we identified that the main source of white noise was the electrical magnetic interference from the environment at frequencies above 50 Hz. The vast majority of the noise signals was removed by filtering out the high-frequency signals. The voltage output signals before and after filtering are shown in blue and red curves, respectively [Fig. 10(a)]. The voltage signals were converted to real-time ISS profiles by low-pass filter [Fig. 10(b)]. Note that the second peaks represented the rectified waveforms.

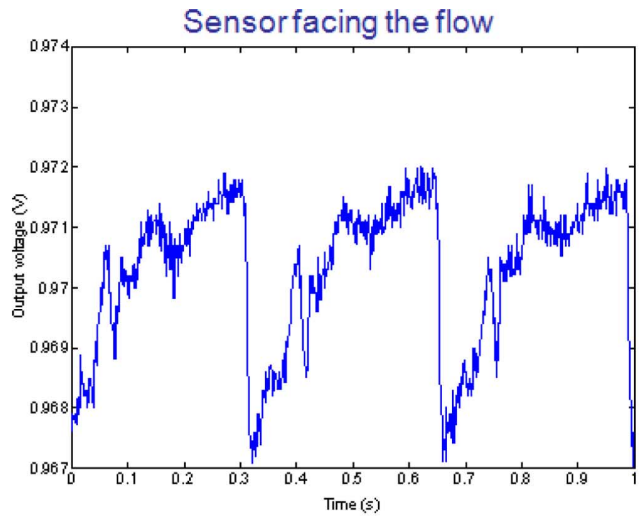

(a)

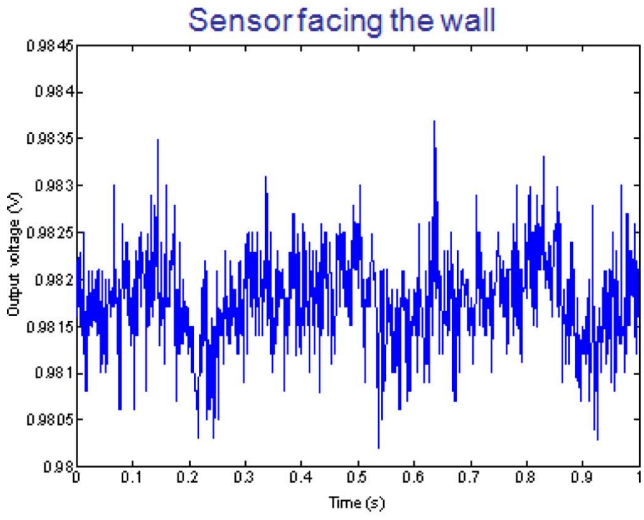

(b)

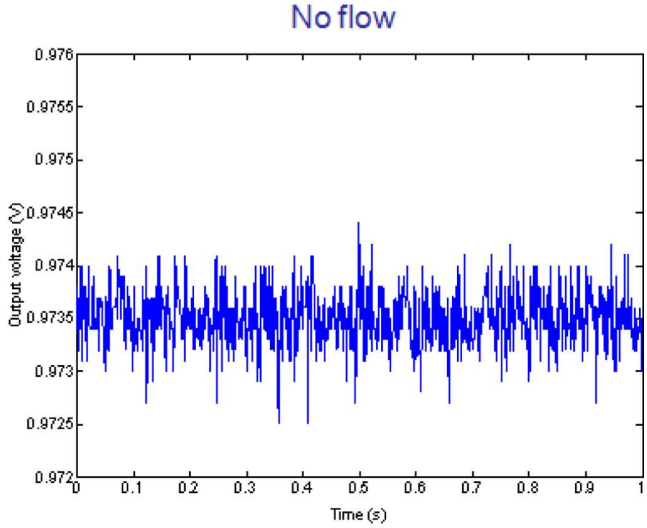

(c)

Fig. 8. Distinct voltage waveforms for different sensor positions. (a) Pulsatile voltage signals were observed when the sensor was facing the flow. (b) As the sensor was steered toward the arterial wall, the signals were distorted. Noise signals were recorded when the sensor was placed against the wall. (c) Voltage signals became flat line with noises when the blood flow ceased.

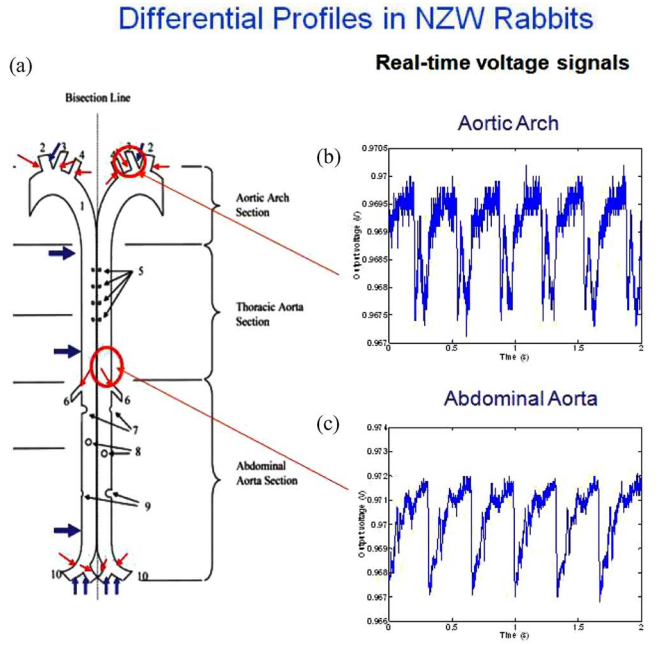

Fig. 9. Pulsatile voltage signals near abdomen versus greater curvature of aortic arch. (a) Diagram (not drawn to scale) illustrated bisection of the aorta and division of aortic segments of the NZW rabbit. 1: the aorta; 2: brachiocephalic trunk; 3: common carotid artery (which sometimes branches from the brachiocephalic trunk); 4: left subclavian artery; 5: dorsal intercostal arteries; 6: celiac artery; 7: cranial mesenteric artery; 8: right and left renal arteries; 9: caudal mesenteric artery; 10: iliac arteries. Red arrows indicate loci where disturbed flow occurred. Blue arrows indicate regions where pulsatile flow developed. (b) Real-time voltage signal acquired near the greater curvature of aortic arch. (c) Real-time voltage signal acquired from the abdominal aorta. The heart rate was at 180 beats/min and the respiratory rate at 30 times/min.

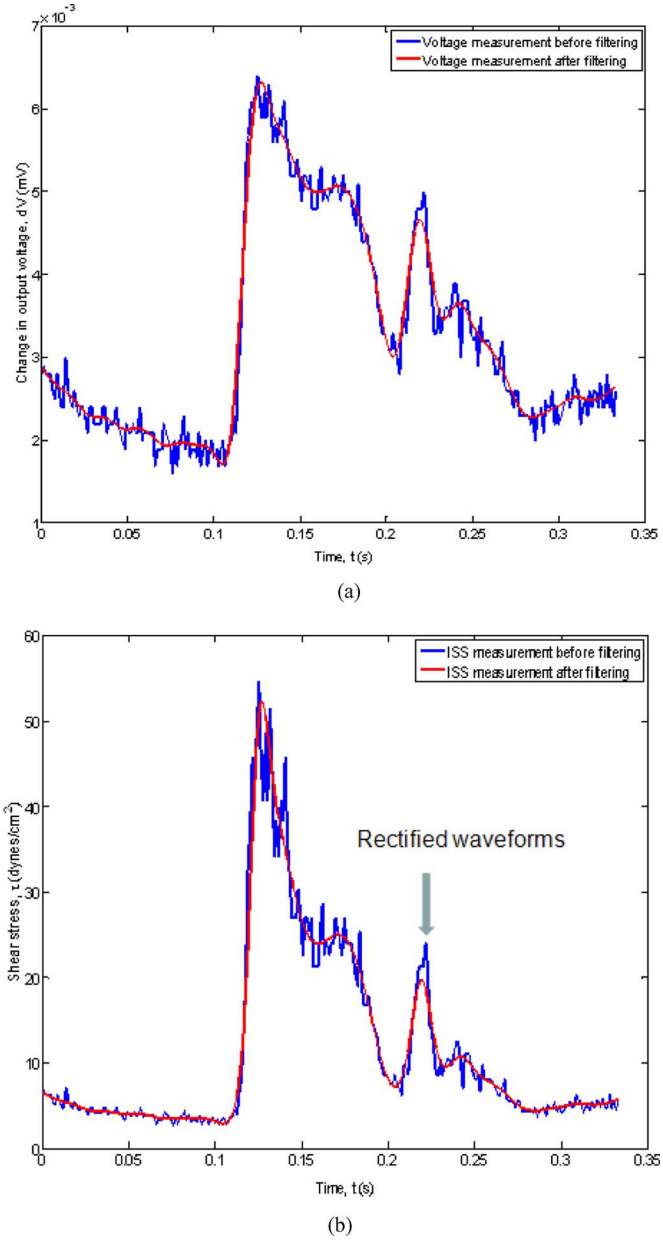

Fig. 10. Wavelet decomposition and low-pass filtering removed most of the noise signals. (a) Voltage output signals before and after filtering. (b) Shear stress profiles converted from the voltage signals before and after filtering.

Real-time ISS was compared with the CFD simulations. Superimposed on the real-time ISS profile were the CFD solutions of ISS and WSS before and after the coaxial wire was located at the center (Fig. 11). The waveform of the real-time ISS closely overlapped with that of the CFD simulations. The computed shear stress profiles were rectified as evidenced by the shown peaks. The rectified waveforms reflected the absolute values during the diastole when flow reversal occurred. The second peak of the pulsatile waveform represented the computed shear stress values during diastole. Due to flow reversal in diastole, the real-time ISS values were influenced by the short-time plateau and trough following the first peak. The real-time systolic ISS measurement peaked at 51.2 dyn·cm^{-2}, while the computed WSS and ISS in the presence of catheter peaked at 47.0 and 102.8 dyn·cm^{-2}, respectively. The peak systolic WSS in the absence of catheter was computed to be 33.2 dyn·cm^{-2}. The WSS values (mean magnitude of $\mathrm{WSS}_{\mathrm{nocatheter}} = 10.1$ dyn·cm^{-2}) were computed to be elevated in the presence of catheter. The difference between the mean magnitudes of $\mathrm{ISS}_{\text{real-time}}$ (11.9 dyn·cm^{-2}) and $\mathrm{WSS}_{\mathrm{catheter}}$ (15.5 dyn·cm^{-2}) was 3.4 dyn·cm^{-2}. Hence, the polymer-based sensors provided a possibility to assess real-time ISS in the abdominal aorta of NZW rabbits.

IV. Discussion

The flexile MEMS-based polymer sensors have enabled us to directly quantify real-time ISS for the first time. We deployed the MEMS sensors to monitor ISS in the abdominal aorta of adult NZW rabbits and demonstrated the possibility to translate the sensors to acquire real-time ISS measurement in the abdominal aorta. Despite numerous CFD solutions for WSS, there has been a paucity of experimental data. A 30% distortion is commonly encountered for experimental intravascular measurements [42]. Distinct from WSS measurement in an *in vitro* bifurcating model [21], the coaxial-wire-based sensors provided a basis for the future intravascular analysis with temporal and spatial resolution.

Despite the difference in magnitude, real-time ISS in the abdominal aorta showed a similar waveform as that of the computed ISS. Several reasons accounted for the difference in

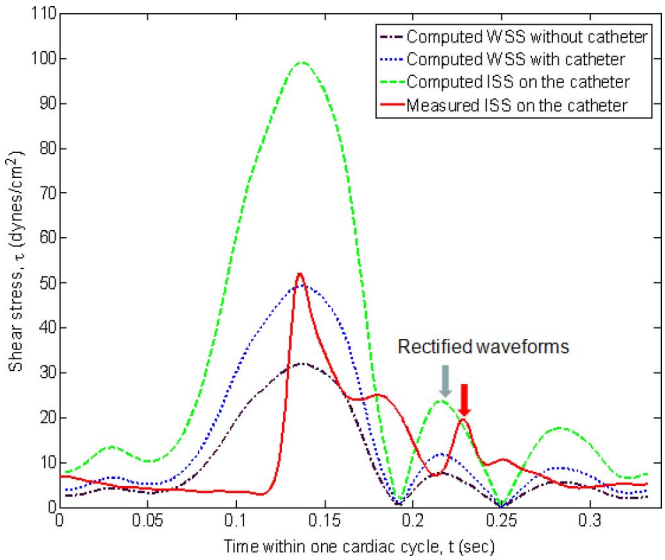

Fig. 11. ISS tracings in one cardiac cycle were compared with CFD solutions. Superimposed on the real-time ISS profile (red solid line) were the CFD solutions of ISS (green dashed line) and WSS before (black dash-dotted line) and after (blue dotted line) the coaxial wire was located at the center. The waveform of the real-time ISS resembled those of the computed despite the difference in magnitude.

magnitude between the experimental and computational data. The degree of eccentricity and the orientation of the sensor strongly influenced the real-time shear stress levels. Also, the Doppler ultrasound velocity profiles were acquired prior to the deployment of coaxial wire. Both the flow rate and shear stress level were reduced after the catheter-based sensor was deployed into the abdominal aorta due to the increase of flow resistance [43]–[46]. The arterial branches also induced focal effects that were not taken into account in our CFD simulation. Furthermore, the non-Newtonian properties of rabbit blood contributed to experimental error in sensor calibration [47]. For a given hematocrit ratio, the apparent viscosity is measured to be smaller in a viscometer than in a conventional capillary tube viscometer [48]. Finally, the CFD simulation considered the arterial wall noncontractile.

Despite the high spatial and temporal resolution of the MEMS sensors, we will need to optimize the packaging and deployment techniques as predicted by the theoretical and CFD analyses. Specifically, ISS assessment could be further optimized by positioning the catheter near the vessel wall using a steerable catheter with a large diameter ratio ($D_{\mathrm{aorta}}/D_{\mathrm{coaxial\ wire}}$). In humans, the diameter ratio could approach to 100 for an aortic inner diameter of 2.5 cm with a catheter outer diameter of 0.254 mm. In this context, we anticipate to further decrease the experimental errors in shear stress assessment by testing the MEMS sensors in a large animal model such as swine.

In the CFD simulation, we simulated a flow situation analogous to the flow in an annular duct [49], [50]. Due to the presence of the catheter, the flow inside the vessel was contracted when the blood enters the annulus. ISS in this study referred to shear stress acting on the surface of the catheter. Rather than measuring WSS, other investigators measured endothelial shear stress (ESS) by using coronary intravascular ultrasound (IVUS) and measurement of coronary blood flow for calculating ESS [51]. However, the velocity gradient near the center would be smaller in the absence than in the presence of IVUS catheter. Thus, the relation between the original WSS and the altered ISS depended on the catheter to vessel diameter ratios ($n = D_{\mathrm{vessel}}/D_{\mathrm{catheter}}$).

The main limitation of the current coaxial-wire-based sensors is to predict the location and time in the cardiac cycle where the flow will be reversed. Ultrasound and echocardiogram have also been used routinely to visualize the contracting heart as well as the superficial arteries such as carotid and femoral arteries. High-frequency ultrasound has also been used to interrogate human abdominal aorta. The use of Doppler ultrasound would reveal flow reversal. However, the small dimension of rabbit abdominal aorta significantly attenuates the spatial resolution. In our future investigation with large animal model, the simultaneous application of abdominal Doppler ultrasound will provide the velocity profile and delineate the cross section of the aorta for the position of the sensor.

In our current study, the use of MEMS sensors alone would not identify the location and duration of the flow reversal, and hence the directional changes in the measured shear stress in complicated arterial configuration. The development of two-sensor system would be able to address the flow reversal by cross correlation between the voltage outputs from the two individual sensors [52]. The cross-correlation approach would provide a basis to assess flow reversal in a well-defined 3-D bifurcation configuration [21], and therefore to assess the flow reversal in the arterial curvature and/or bifurcations and branching points.

Angiogram along with contrast dye has been the routine procedure in the cardiac catheterization laboratory. In humans, the procedure allows for visualization of catheter deployment into the coronary arteries and detection of arterial plaques. In our NZW rabbit model, the procedure not only allowed for visualization of the sensors but also the 3-D geometry of the aorta for CFD boundary condition.The biplane X-ray angiography would be a good solution for the future study to acquire precise measurements of the vessel cross-sectional area and the sensor position in relation to the vessel diameter.

The signal-to-noise ratio was important for *in vivo* application. The sensing element was microfabricated by depositing Ti/Pt, providing a good biocompatibility and sensitivity [25]. The noise floor or the current voltage output measurement was $\sim$0.5 mV, which was filtered by utilizing the wavelet decomposition and a low-pass filter. Given that the sampling rate was 800 Hz, the signals were decomposed to signal frequencies falling in the following ranges: 0–25, 25–50, 50–100, 100–200, and 200–400 Hz. After identifying the frequencies of the white noise above 50 Hz, a low-pass filter was applied to remove the high-frequency noise. The application of wavelet decomposition and low-pass filtering demonstrated the capability to distinguish the noise background from the electrical signal measurements.

In conclusion, this pilot study enabled us to assess ISS in the animal models. The feasibility of translating the MEMS device for real-time analysis paves the way to conduct long-term

follow-up of voltage output waveform changes in our animal model in response to hypercholesterolemic diet. The flexible MEMS sensors can also be calibrated for changes in focal pressure, temperature, and flow rates. Hence, the coaxial-wire-based MEMS sensors open a new door to link quantitative measurement with cardiovascular system.

ACKNOWLEDGMENT

The authors would like to thank P. Sun for the help with the noise filtering.

REFERENCES

[1] Y. S. Chatzizisis, A. U. Coskun, M. Jonas, E. R. Edelman, C. L. Feldman, and P. H. Stone, "Role of endothelial shear stress in the natural history of coronary atherosclerosis and vascular remodeling—Molecular, cellular, and vascular behavior," *J. Amer. Coll. Cardiol.*, vol. 49, pp. 2379–2393, 2007.

[2] J. R. Hove, R. W. Koster, A. S. Forouhar, G. Acevedo-Bolton, S. E. Fraser, and M. Gharib, "Intracardiac fluid forces are an essential epigenetic factor for embryonic cardiogenesis," *Nature*, vol. 421, pp. 172–177, 2003.

[3] S. Nonaka, H. Shiratori, Y. Saijoh, and H. Hamada, "Determination of left-right patterning of the mouse embryo by artificial nodal flow," *Nature*, vol. 418, pp. 96–99, 2002.

[4] K. Yamamoto, T. Sokabe, T. Watabe, K. Miyazono, J. K. Yamashita, S. Obi, N. Ohura, A. Matsushita, A. Kamiya, and J. Ando, "Fluid shear stress induces differentiation of Flk-1-positive embryonic stem cells into vascular endothelial cells in vitro," *Amer. J. Physiol. Heart Circ. Physiol.*, vol. 288, pp. H1915–H1924, 2005.

[5] H. Wang, G. M. Riha, S. Yan, M. Li, H. Chai, H. Yang, Q. Yao, and C. Chen, "Shear stress induces endothelial differentiation from a murine embryonic mesenchymal progenitor cell line," *Arterioscler. Thromb. Vasc. Biol.*, vol. 25, pp. 1817–1823, 2005.

[6] R. Ross, "Atherosclerosis is an inflammatory disease," *Amer. Heart J.*, vol. 138, pp. S419–S420, 1999.

[7] J. Niebauer and J. P. Cooke, "Cardiovascular effects of exercise: Role of endothelial shear stress," *J. Amer. Coll. Cardiol.*, vol. 28, pp. 1652–1660, 1996.

[8] G. W. De Keulenaer, D. C. Chappell, N. Ishizaka, R. M. Nerem, R. W. Alexander, and K. K. Griendling, "Oscillatory and steady laminar shear stress differentially affect human endothelial redox state: Role of a superoxide-producing NADH oxidase," *Circ. Res.*, vol. 82, pp. 1094–1101, 1998.

[9] J. Hwang, M. Rouhanizadeh, R. T. Hamilton, T. C. Lin, J. P. Eiserich, H. N. Hodis, and T. K. Hsiai, "17 beta-Estradiol reverses shear-stress-mediated low density lipoprotein modifications," *Free Radical. Biol. Med.*, vol. 41, pp. 568–578, 2006.

[10] P. H. Stone, A. U. Coskun, S. Kinlay, M. E. Clark, M. Sonka, A. Wahle, O. J. Ilegbusi, Y. Yeghiazarians, J. J. Popma, J. Orav, R. E. Kuntz, and C. L. Feldman, "Effect of endothelial shear stress on the progression of coronary artery disease, vascular remodeling, and in-stent restenosis in humans—*In vivo* 6-month follow-up study," *Circulation*, vol. 108, pp. 438–444, 2003.

[11] Y. S. Chatzizisis, M. Jonas, A. U. Coskun, R. Beigel, B. V. Stone, C. Maynard, R. G. Gerrity, W. Daley, C. Rogers, E. R. Edelman, C. L. Feldman, and P. H. Stone, "Prediction of the localization of high-risk coronary atherosclerotic plaques on the basis of low endothelial shear stress—An intravascular ultrasound and histopathology natural history study," *Circulation*, vol. 117, pp. 993–1002, 2008.

[12] T. W. Taylor and T. Yamaguchi, "3-dimensional simulation of blood-flow in an abdominal aortic-aneurysm—Steady and unsteady flow cases," *J. Biomech. Eng., Trans. ASME*, vol. 116, pp. 89–97, 1994.

[13] M. L. Raghavan, D. A. Vorp, M. P. Federle, M. S. Makaroun, and M. W. Webster, "Wall stress distribution on three-dimensionally reconstructed models of human abdominal aortic aneurysm," *J. Vasc. Surg.*, vol. 31, pp. 760–769, 2000.

[14] E. J. Roschke and E. C. Harrison, "Fluid shear stress in prosthetic heart valves," *J. Biomech.*, vol. 10, pp. 299–311, 1977.

[15] Y. J. Gu, P. W. Boonstra, R. Graaff, A. A. Rijnsburger, H. Mungroop, and W. van Oeveren, "Pressure drop, shear stress, and activation of leukocytes during cardiopulmonary bypass: A comparison between hollow fiber and flat sheet membrane oxygenators," *Artif. Organs*, vol. 24, pp. 43–48, 2000.

[16] X. W. Song, A. L. Throckmorton, H. G. Wood, J. F. Antaki, and D. B. Olsen, "Quantitative evaluation of blood damage in a centrifugal VAD by computational fluid dynamics," *J. Fluids Eng., Trans. ASME*, vol. 126, pp. 410–418, 2004.

[17] T. K. Hsiai, J. Hwang, M. L. Barr, A. Correa, R. Hamilton, M. Alavi, M. Rouhanizadeh, E. Cadenas, and S. L. Hazen, "Hemodynamics influences vascular peroxynitrite formation: Implication for low-density lipoprotein apo-B-100 nitration," *Free Radic. Biol. Med.*, vol. 42, pp. 519–529, 2007.

[18] J. Hwang, M. H. Ing, A. Salazar, B. Lassegue, K. K. Griendling, M. Navab, A. Sevanian, and T. K. Hsiai, "Pulsatile vs. oscillatory shear stress regulates NADPH oxidase system: Implication for native LDL oxidation," *Circ. Res.*, vol. 93, pp. 1225–1232, 2003.

[19] C. M. Ho and Y. C. Tai, "Micro-electro-mechanical-systems and fluid flows," *Annu. Rev. Fluid Mech.*, vol. 30, pp. 579–612, 1998.

[20] G. Soundararajan, M. M. Rouhanizadeh, H. Yu, E. S. Kim, and T. K. Hsiai, "MEMS sensors for microcirculation," *Sens. Actuators*, vol. 118, pp. 25–32, 2005.

[21] M. Rouhanizadeh, G. Soundararajan, D. Ascara, R. Lo, F. Browand, and T. Hsiai, "MEMS sensors to resolve spatial variations in shear stress in a 3-D bifurcation model," *IEEE Sens. J.*, vol. 6, no. 1, pp. 78–88, Feb. 2006.

[22] C. Liu, J. B. Huang, Z. J. Zhu, F. K. Jiang, S. Tung, Y. C. Tai, and C. M. Ho, "Micromachined flow shear-stress sensor based on thermal transfer principles," *J. Microelectromech. Syst.*, vol. 8, pp. 90–99, 1999.

[23] E. F. Meng and Y. C. Tai, "Polymer MEMS for micro fluid delivery systems," *Abstracts Papers Amer. Chem. Soc.*, vol. 226, pp. U383–U383, 2003.

[24] C. Liu, "Recent developments in polymer MEMS," *Adv. Mater.*, vol. 19, pp. 3783–3790, 2007.

[25] H. Yu, L. Ai, M. Rouhanizadeh, D. Patel, E. S. Kim, and T. K. Hsiai, "Flexible polymer sensors for in vivo intravascular shear stress analysis," *IEEE/ASME J. Microelectromech. Syst.*, vol. 17, no. 5, pp. 1178–1186, Oct. 2008.

[26] T. D. Kim, T. W. Seo, and A. I. Barakat, "Numerical simulations of fluid mechanical interactions between two abdominal aortic branches," *Korea-Australia Rheol. J.*, vol. 16, pp. 75–83, 2004.

[27] Y. A. Ermolaev and M. Ra, "Potential of aortic current in rabbit," *Biulleten Eksperimentalnol Biol. I Med.*, vol. 77, pp. 6–8, 1974.

[28] *GAMBIT 2.3 User's Guide*, F. I. Fluent, Inc., Lebanon, NH, 2006.

[29] P. W. Longest, C. Kleinstreuer, G. A. Truskey, and J. R. Buchanan, "Relation between near-wall residence times of monocytes and early lesion growth in the rabbit aorto-celiac junction," *Ann. Biomed. Eng.*, vol. 31, pp. 53–64, 2003.

[30] G. Lorenzini, "Blood velocity field numerical assessment using a GPL code in case of intravascular Doppler catheter affections: Comparative analysis of different rheological models," *J. Biomech.*, vol. 38, pp. 2058–2069, 2005.

[31] R. C. Armstrong, R. B. Bird, and O. Hassager, "Dynamics of polymeric liquids," in *Fluid Mechanics*. vol. 1, New York: Wiley, 1977, p. 470.

[32] D. V. Boger, "Viscoelastic flows through contractions," *Annu. Rev. Fluid Mech.*, vol. 19, pp. 157–182, 1987.

[33] J. R. Buchanan, C. Kleinstreuer, S. Hyun, and G. A. Truskey, "Hemodynamics simulation and identification of susceptible sites of atherosclerotic lesion formation in a model abdominal aorta," *J. Biomech.*, vol. 36, pp. 1185–1196, 2003.

[34] *FLUENT 6.2 User's Guide*, Inc., F. I. Fluent, Lebanon, NH, 2006.

[35] R. K. Banerjee, L. H. Back, and M. R. Back, "Effects of diagnostic guidewire catheter presence on translesional hemodynamic measurements across significant coronary artery stenoses," *Biorheology*, vol. 40, pp. 613–635, 2003.

[36] R. K. Banerjee, L. H. Back, M. R. Back, and Y. I. Cho, "Catheter obstruction effect on pulsatile flow rate-pressure drop during coronary angioplasty," *J. Biomech. Eng., Trans. ASME*, vol. 121, pp. 281–289, 1999.

[37] A. S. Roy, L. H. Back, and R. K. Banerjee, "Guidewire flow obstruction effect on pressure drop-flow relationship in moderate coronary artery stenosis," *J. Biomech.*, vol. 39, pp. 853–864, 2006.

[38] W. Hillewaert, K. Courtens, M. McLaughlin, J. Wauters, A. Wilmer, B. Bijnens, P. Claus, P. Verdonck, P. Devos, and P. Segers, "Numerical assessment of the impact of a flow wire on its velocity measurements," *Ultrasound Med. Biol.*, vol. 32, pp. 1025–1036, 2006.

[39] R. Krams, J. J. Wentzel, I. Cespedes, R. Vinke, S. Carlier, A. F. Van Der Steen, C. T. Lancee, and C. J. Slager, "Effect of catheter placement on 3-D velocity profiles in curved tubes resembling the human coronary system," *Ultrasound Med. Biol.*, vol. 25, pp. 803–810, 1999.

[40] L. Ai, H. Yu, R. Li, H. Yu, A. Paraboschi, and T. Hsiai, "Optimization of intravascular shear stress assessment in the abdominal aorta of New Zealand White Rabbits," submitted for publication.
[41] M. Rouhanizadeh, T. C. Lin, D. Arcas, J. Hwang, and T. K. Hsiai, "Spatial variations in shear stress in a 3-D bifurcation model at low Reynolds numbers," *Ann. Biomed. Eng.*, vol. 33, pp. 1360–1374, 2005.
[42] D. N. Ku, "Blood flow in arteries," *Annu. Rev. Fluid Mech.*, vol. 29, pp. 399–434, 1997.
[43] R. K. Dash, G. Jayaraman, and K. N. Mehta, "Estimation of increased flow resistance in a narrow catheterized artery—A theoretical model," *J. Biomech.*, vol. 29, pp. 917–930, 1996.
[44] A. S. Roy, R. K. Banerjee, L. H. Back, M. R. Back, S. Khoury, and R. W. Millard, "Delineating the guide-wire flow obstruction effect in assessment of fractional flow reserve and coronary flow reserve measurements," *Amer. J. Physiol. Heart Circ. Physiol.*, vol. 289, pp. H392–H397, 2005.
[45] J. J. Wentzel, R. Krams, A. F.W. Van Der Steen, W. Li, E. I. Cespedes, N. Bom, and C. J. Slager, "Disturbance of 3-D velocity profiles induced by IVUS catheter, evaluation with computational fluid dynamics," *Comput. Cardiol.*, vol. 24, pp. 597–600, 1997.
[46] J. W. Doucette, P. D. Corl, H. M. Payne, A. E. Flynn, M. Goto, M. Nassi, and J. Segal, "Validation of a Doppler guide wire for intravascular measurement of coronary-artery flow velocity," *Circulation*, vol. 85, pp. 1899–1911, 1992.
[47] R. M. Berne and M. N. Levy, *Cardiovascular Physiology*, 8th ed. St. Louis, MO, Mosby, 2001.
[48] M. N. Levy and L. Share, "The influence of erythrocyte concentration upon the pressure-flow relationships in the dog's hind limb," *Circ. Res.*, vol. 1, pp. 247–255, 1953.
[49] R. K. Shah, *Laminar Flow Forced Convection in Ducts*. New York: Academic, 1978.
[50] S. Bhattach and C. Tiu, "Developing pressure profiles for non-Newtonian flow in an annular duct," *AIChE J.*, vol. 20, pp. 154–158, 1974.
[51] P. H. Stone, A. U. Coskun, S. Kinlay, M. E. Clark, M. Sonka, A. Wahle, O. J. Ilegbusi, Y. Yeghiazarians, J. J. Popma, J. Orav, R. E. Kuntz, and C. L. Feldman, "Effect of endothelial shear stress on the progression of coronary artery disease, vascular remodeling, and in-stent restenosis in humans: In vivo 6-month follow-up study," *Circulation*, vol. 108, pp. 438–444, 2003.
[52] B. Van Oudheusden, "Silicon thermal flow sensor with a two-dimensional direction sensitivity," *Meas. Sci. Technol.*, vol. 1, pp. 565–575, 1990.

Lisong Ai received the B.S. degree in mechanical engineering from Zhejiang University, Hangzhou, China, in 2002, and the M.S. degree in mechanical engineering from the University of California-Riverside, Riverside, in 2005. He is currently working toward the Ph.D. degree in the Department of Biomedical Engineering and the Division of Cardiovascular Medicine, University of Southern California, Los Angeles.

His current research interests include biomicroelectromechanical system (BioMEMS) sensors for the diagnosis of cardiovascular diseases and numerical simulation of blood flow in arteries.

Hongyu Yu (M'03) received the B.S. and M.S. degrees in electronics engineering from Tsinghua University, Beijing, China, in 1997 and 2000, respectively, and the Ph.D. degree in electrical engineering from the University of Southern California, Los Angeles, in 2005.

He holds the joint position between the School of Earth and Space Exploration and Electrical Engineering Department at Arizona State University, Tempe, and is engaged in developing microelectromechanical system (MEMS) for earth and space applications. His current research interests include seismometers, wireless sensing systems, microfluidic analysis systems, acoustic transducers, and microfuel cells. The goal of his research is to provide miniaturized platforms and instruments for earth, planet, and space scientists to study variety of projects, such as seismology, biogeochemistry, astrobiology, and volcanology.

Wangde Dai received the M.D. degree from Shanghai Medical University, Shanghai, China, in 1999.

For two years, he was a Research Fellow in the Vascular Gene Therapy Laboratory, Department of Surgery/Vascular Division, Keck School of Medicine, University of Southern California, Los Angeles, where he is currently a Research Assistant Professor of medicine. In 2002, he joined as a Research Fellow at the Heart Institute, Good Samaritan Hospital, Los Angeles, where he is a Research Scientist. He has been involved in the studies including cell transplantation therapy in the heart and vasculature and development of therapies for limiting myocardial infarct size and protection of cardiac function following coronary artery occlusion in rat and mice myocardial infarction model for the last nine years.

Sharon L. Hale graduated from Cornell University, Ithaca, NY.

She is a Senior Researcher at the Heart Institute, Good Samaritan Hospital, Los Angeles, CA. She has authored or coauthored more than 100 articles published in the field of cardiovascular research.

Robert A. Kloner received the M.D. in the Honors Program in Medical Education and Ph.D. degrees from the Northwestern University Medical School, Chicago, IL.

He is a Professor of medicine in the Cardiovascular Division, Keck School of Medicine, University of Southern California, Los Angeles. He is also the Director of Research at the Heart Institute of Good Samaritan Hospital, Los Angeles, and an attending cardiologist at Los Angeles County. He was an Assistant Professor and then an Associate Professor of medicine at Harvard Medical School, and an attending cardiologist at Brigham and Women's Hospital. His current research interests include cardiac cell transplantation, protection of ischemic myocardium, development of therapies for limiting myocardial infarct size, cardiac function following coronary artery occlusion, the effect of toxins on the heart, including the effect of air pollution on the heart, preventative cardiology, hypertension, and PDE5 inhibition. He has authored or coauthored 538 original papers in peer-reviewed journals, 207 chapters or monographs, and over 430 abstracts. He is the author and the editor of 18 medical texts including *Cardiovascular Trials Reviews, The Guide to Cardiology* (three editions)*, Stunned Myocardium, Ischemic Preconditioning, VIAGRA, and Heart Disease and Erectile Dysfunction*, and three novels—*The Beta Virus, Mind Cure, and The Deity Genes.*

Prof. Kloner is a member of the Alpha Omega Alpha Honor Society. He is a Fellow of the American College of Cardiology, an Inaugural Fellow of the Council on Basic Cardiovascular Sciences of the American Heart Association (AHA), and was elected to the American Society of Clinical Investigation.

Tzung K. Hsiai received the B.S. degree from Columbia University, New York, the M.D. degree from the University of Chicago, Chicago, IL, and the Ph.D. degree in biomedical engineering from the School of Medicine, University of California (UCLA), Los Angeles, in 2002.

He was a Postgraduate Medical Trainee and a National Institutes of Health (NIH) National Research Service Award (NRSA) Cardiology Fellow at the School of Medicine, UCLA. He is currently with the Department of Biomedical Engineering and Cardiovascular Medicine, University of Southern California, Los Angeles.

Dr. Hsiai is a Fellow of the American College of Cardiology. He is the recipient of the National Institutes of Health Physician Scientist Career Development Award and the American Heart Association John J. Simpson Outstanding Research Achievement Award.